High-resolution angle-resolved photoemission spectra from Ni(100): Matrix element effects and spin-resolved initial and final state bands

S. Sahrakorpi and M. Lindroos
Institute of Physics, Tampere University of Technology, 33101 Tampere, Finland
and Department of Physics, Northeastern University, Boston, Massachusetts 02115

A. Bansil
Department of Physics, Northeastern University, Boston, Massachusetts 02115

(Received 18 July 2001; revised manuscript received 24 May 2002; published 16 December 2002)

We have carried out extensive one- and three-step angle-resolved photoemission spectroscopy (ARPES) intensity computations on Ni(100) within the band theory framework based on the local spin-density approximation. The results show a good overall level of accord with the recent high-resolution ARPES experiments on Ni(100) which probe the majority- and minority-spin Σ_1 band along the Γ-K direction near the Fermi energy (E_F), uncertainties inherent in our first-principles approach notwithstanding. The $\mathbf{k}_\parallel$ and energy dependencies of various spectral features are delineated in terms of the interplay between changes in the initial- and final-state bands and the associated transition matrix elements. The remarkable decrease observed with decreasing $k_\parallel$ in the ARPES intensity of the majority-spin Σ_1 band as it disperses below the E_F as well as an enhanced spin polarization of the photoemitted electrons from the E_F is shown to arise from the presence of a band gap in the final-state spectrum.

DOI: 10.1103/PhysRevB.66.235107 PACS number(s): 79.60.−i, 71.20.Be, 75.25.+z, 85.75.−d

I. INTRODUCTION

Recent advances in energy and momentum resolution in angle-resolved photoemission experiments have made it increasingly possible to probe a wider range of problems involving the electronic and magnetic structures of materials via this technique. In this connection, Ni is of interest not only as an archetype magnetic system, but also because Ni and its alloys are attractive in magnetoelectronics applications due to their interesting magnetoresistive properties driven by differences in the behavior of majority and minority electrons in the vicinity of the Fermi energy.[1] These considerations as well as an intrinsic interest in understanding magnetic phenomena in general have motivated numerous theoretical and experimental investigations of Ni and its alloys.[2–10]

With this backdrop in mind, our purpose in this article is to confront first-principles theoretical predictions of the spin-resolved photointensities in Ni(100) with the corresponding experimental measurements. Specifically, we consider the very recent high-resolution angle-resolved photoemission spectroscopy(ARPES) study of Ref. 8 which investigates the majority and minority spin Σ_1 bands along the Γ-K direction in the Brillouin zone (BZ) by using 44 eV photons and shows dramatic variations with $\mathbf{k}_\parallel$ in the spectral intensity of the majority band and a substantially enhanced spin polarization of the photoemitted electrons from the E_F. To this end, we have carried out extensive one-step[11–15] as well as three-step[16–23] ARPES computations from Ni(100) by simulating the conditions of Ref. 8 with respect to the energy and polarization of the incident light and other experimental parameters. Note that, although the one-step approach provides a more satisfactory description of the photoemission process, the fact that the processes of excitation, transport, and ejection of the electron are treated as a single quantum-mechanical event tends to make it somewhat difficult to identify the origin of specific features in the computed spectra. In contrast, the three-step model handles different aforementioned components of the photoemission process separately, and therefore, it more easily allows insight into how spectra are connected with ingredients such as the initial- and final-state bands and the transition matrix elements which go into the three-step computation explicitly. Accordingly, in keeping with the focus of this article on trying to understand the nature and origin of various ARPES features, much of our analysis invokes the three-step results, although the one-step calculations yield similar conclusions.

An outline of this article is as follows. The introductory remarks are followed in Sec. II with comments on the methodology used. Although the formulation of the one- and three-step models is well described in the literature, for our purposes of analyzing the roles of the initial- and final-state bands and the transition matrix elements, we use a somewhat simplified three-step approach which is outlined. Section III goes over computational issues. The results are presented and discussed in Sec. IV which is subdivided into four parts. Section IV A undertakes a direct comparison between the computed and measured ARPES spectra from Ni(100). Salient features of the initial- and final-state bands and the transition matrix elements are discussed in Section IV B. This then allows us to proceed in Section IV C with the analysis of the various observed features in the spectra including the $\mathbf{k}_\parallel$ and energy dependencies of the majority and minority band intensities. Section IV D delineates changes in the character of the initial states over the $\mathbf{k}_\parallel$ and energy region of interest. Finally, Sec. V summarizes the conclusions of this study. The Korringa-Kohn-Rostoker(KKR) formulation of the momentum matrix element for a general lattice is given in the Appendix and will be useful in analyzing ARPES intensities in complex materials along the present lines.

II. METHODOLOGY

In the one-step model of photoemission,[11,12] which we have recently extended to consider arbitrarily complex unit-cell materials,[13–15] the angle-resolved photointensity from initial states at energy E is given by

$$I(E,h\nu,\mathbf{k}_\parallel) = -\frac{1}{\pi}\mathrm{Im}\langle \mathbf{k}_\parallel | G_2^+(E+h\nu)\Delta G_1^+(E)\Delta^\dagger \times G_2^-(E+h\nu)|\mathbf{k}_\parallel\rangle, \quad (1)$$

where $\mathbf{k}_\parallel$ is the component of the measured free-electron final-state momentum parallel to the surface and G_2 and G_1 are the retarded (+) and advanced (−) one-electron Green functions. $\Delta = e\hbar/2mc(\mathbf{p}\cdot\mathbf{A}+\mathbf{A}\cdot\mathbf{p})$ is the interaction Hamiltonian in terms of the vector potential $\mathbf{A}$ of the incident photon field at energy $h\nu$ and the electron momentum operator $\mathbf{p}$. As already pointed out, the three-step model[16–24] is of interest in interpreting spectral features. To this end, Eq. (1) can be cast in the spirit of the three-step model to obtain the photointensity *within* the solid as[22]

$$P(E,h\nu) \propto \sum_{f,i}^{\sigma} \int d\mathbf{k} |\langle \Psi_f^\sigma | \Delta | \Psi_i^\sigma \rangle|^2 A_f^\sigma(E+h\nu) A_i^\sigma(E), \quad (2)$$

in terms of the *bulk* initial- and final-state wave functions Ψ_i and Ψ_f and the one-particle spectral functions A_i and A_f. The superscript σ is the spin index. A form more suitable for obtaining ARPES spectra is

$$I(E,h\nu,\mathbf{k}_\parallel) \propto \sum_{\mathbf{k}_\perp \in BZ} \sum_{f,i}^{\sigma} \Theta(\mathbf{v}_f\cdot\mathbf{n}) M_{f,i}^\sigma(\mathbf{k}_\parallel,\mathbf{k}_\perp)^2 \times \frac{\Sigma_f''}{[E+h\nu-E_f^\sigma(\mathbf{k}_\parallel,\mathbf{k}_\perp)]^2+\Sigma_f''^2} \times \frac{\Sigma_i''}{[E-E_i^\sigma(\mathbf{k}_\parallel,\mathbf{k}_\perp)]^2+\Sigma_i''^2} \quad (3)$$

where the crystal momentum $\mathbf{k}$ is decomposed into components $\mathbf{k}_\parallel$ and $\mathbf{k}_\perp$ parallel and perpendicular to the crystal surface, respectively. The summation is limited to $\mathbf{k}_\perp$ values in the first BZ. $M_{f,i}^\sigma(\mathbf{k}_\parallel,\mathbf{k}_\perp) \equiv |\mathbf{A}\cdot\langle \Psi_f^\sigma|\mathbf{p}|\Psi_i^\sigma\rangle|$ is the photoemission matrix element wherein the polarization of the incident light field is taken into account. The formalism for evaluating $\langle \Psi_f^\sigma|\mathbf{p}|\Psi_i^\sigma\rangle$ is outlined in the Appendix. The step function $\Theta(\mathbf{v}_f\cdot\mathbf{n})$ restricts the transitions to only those in which the photoelectron (with group velocity $\mathbf{v}_f$) is traveling towards the surface (with normal $\mathbf{n}$). The finite lifetimes of the initial and final states are described by replacing the spectral functions A_i and A_f by Lorentzians via the imaginary parts of the initial- and final-state self-energies Σ_i'' and Σ_f''.

It should be noted that Eq. (3) does not describe the transport and ejection of the photoelectron through the surface properly. However, the similarity between the one-step and three-step results (see Sec. IV A below) indicates that over the relatively small $\mathbf{k}_\parallel$ and energy ranges considered in this article, these contributions do not vary rapidly. In any event, our use of Eq. (3) is meant largely to gain insight into the ARPES spectra which we have computed as well within the one-step framework. One aspect of Eq. (3) is particularly noteworthy. For a given crystal momentum $\mathbf{k}$, the Bloch wave function of the excited electron, $\Psi_f(\mathbf{k},\mathbf{r}) = \Sigma_{\mathbf{G}} u_{f,\mathbf{k},\mathbf{G}} e^{(\mathbf{k}+\mathbf{G})\cdot\mathbf{r}}$, in general, contains umklapp contributions from plane waves with momenta $\mathbf{k}+\mathbf{G}$, for all reciprocal-lattice vectors $\mathbf{G}$. The ARPES experiment of course measures only plane waves with a specific $\mathbf{k}_\parallel$ determined by the solid angle of the detector and the kinetic energy of the outgoing electron. The so-called *primary cone* contribution to the ARPES spectrum will arise from the components of the final-state wave function with $\mathbf{G}_\parallel = \mathbf{0}$.[25] Photoelectrons with $\mathbf{G}_\parallel \neq \mathbf{0}$ momentum components must undergo an umklapp scattering process in order to reach the detector; intensity of such *secondary cone* photoelectrons is, therefore, highly reduced.[25] In the specific case considered here, this constraint can be adequately included in the three-step calculations by restricting the $k_\perp$ summation in Eq. (3) appropriately; the specifics are discussed in Sec. IV B below. More generally, however, one would need to match the final-state wave function to a plane-wave expansion,[20,26,27] in order to select the appropriate primary cone electron beam.

III. COMPUTATIONAL DETAILS

The spin-polarized electronic structure of Ni was first obtained self-consistently using the semirelativistic KKR band-structure scheme where exchange-correlation effects are incorporated within the local spin-density (LSD) approximation;[28,29] for details of our KKR methodology for metals and alloys, see Refs. 30–32. The fcc lattice constant of a=6.594 a.u. was determined by minimizing the total energy. Self-consistency cycles for the crystal potential were repeated until the difference between the new and old potentials was less than 0.1 mRy so that a high degree of convergence was achieved. Since we require final states as high as ~60 eV above the Fermi level, $l_{max}=4$ cutoff was used. The evaluation of the energy distribution curves (EDC's) was next carried out for $\mathbf{k}_\parallel$ along the [011] direction over the range 0.5–1.1 Å^{-1} in steps of 0.025 Å^{-1}. The input to the one-step computations in this connection mainly consists of the crystal potential and various relevant experimental parameters such as $\mathbf{k}_\parallel$ and photon energy.

We outline some further details of the three-step calculations as follows. For this purpose, at any given $\mathbf{k}_\parallel$, initial- and final-state bands and wave functions were computed over a dense mesh along the $\mathbf{k}_\perp$ direction of step size 0.0045 Å^{-1} extending to the BZ boundaries. With this information, the momentum matrix elements were computed for all relevant transitions using the formulas outlined in the Appendix. The EDC's were then obtained by carrying out the $\mathbf{k}_\perp$ integration in Eq. (3). The particular experimental ARPES setup of Ref. 8 implies specific constraints on the allowed initial and final states. First, since the detector lies in the [011] mirror plane, the final state must possess even parity with respect to this plane in order to be observable.[33] Second, the experiment employs *p*-polarized light such that the electric-field vector also lies in this mirror plane. It can

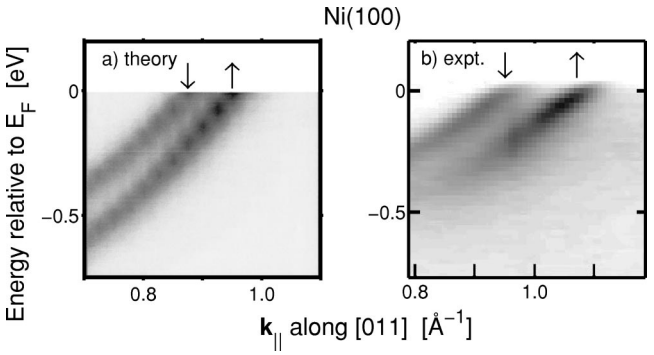

FIG. 1. Theoretical (three-step) and experimental majority (↑) and minority (↓) ARPES intensities for emission from the Σ_1 band in Ni(100) for $\mathbf{k}_{\|}$ along the [011] direction are compared in gray scale plots; black denotes highs. Experimental results are taken from Ref. 8. Zero of energy is the Fermi energy, E_F.

then be shown that only initial states with even parity with respect to the mirror plane can be excited. For the energies and $k_{\|}$ values of interest in this article this reduces possible initial states to the minority and majority Σ_1 states in the vicinity of the E_F. The aforementioned constraints have been incorporated in the computed spectra.

Several sets of one- and three-step computations over the 40–47 eV photon energy range were carried out. With uncertainties of a few eV's with respect to the final-state energies inherent in the first-principles computations, and the fact that the results for $h\nu=43$ eV seem to be the most representative of the experimental spectra of Ref. 8, all theoretical one- and three-step results shown in this article are for $h\nu=43$ eV. The broadening parameters used for the final and initial states are $\Sigma_f''=1.0$ eV and $\Sigma_i''=0.05$ eV. The choice of $\Sigma_i''=0.05$ eV is in line with the observed widths of the ARPES peaks in the high-resolution spectra of Ref. 8.[34] The value $\Sigma_f''=1.0$ eV, however, is more tricky and this point is discussed further in Sec. IV C below. Finally, we note that the self-consistent LSD potential for Ni yields an exchange splitting of 0.48 eV for the Σ_1 d band at the Γ point which is well known to be too large by about a factor of 2.[35] We have attempted to correct this by rigidly shifting our minority spin potential such that the aforementioned exchange splitting is reduced to 0.21 eV at $k_{\|}=0.875$ Å^{-1} (the point where the minority spin band crosses the E_F) which is close to the corresponding experimental value of 0.23 eV.

IV. RESULTS AND DISCUSSION

A. Comparison between experimental and theoretical ARPES spectra from Ni(100)

Figure 1 presents theoretical three-step ARPES spectra over a $\mathbf{k}_{\|}$ range along [011] comparable to the measurements of Ref. 8 and displays a good overall level of accord between theory and experiment. In particular, the computed spectra, much like the experimental results, display the rapid attenuation of the majority band as it disperses below the E_F, while the intensity of the minority band stays more or less constant. At the E_F, the calculated minority band intensity is

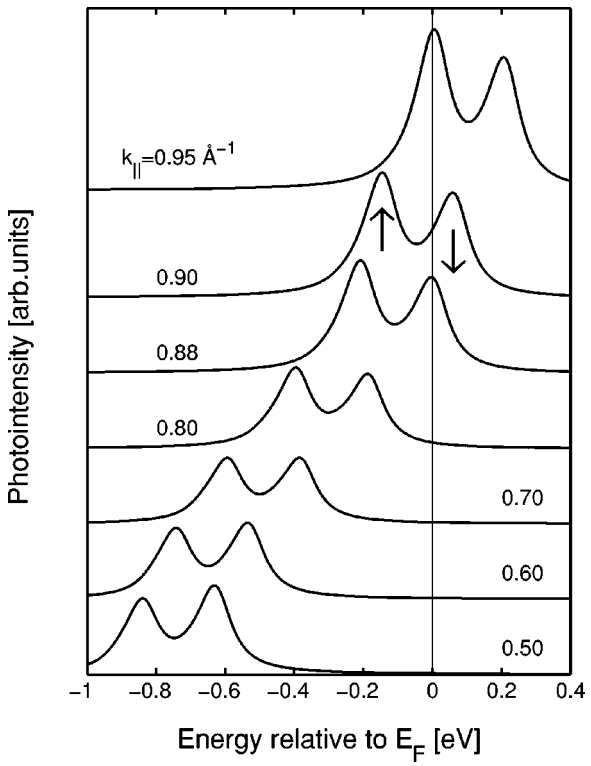

FIG. 2. Theoretical (three-step) energy distribution curves (EDC's) from Ni(100) for $\mathbf{k}_{\|}$ along the [011] direction for $k_{\|}$ ranging from 0.50–0.95 Å^{-1}. Spectra have not been convoluted with the Fermi function. Majority and minority peaks are marked by arrows.

correctly predicted to be significantly smaller than that of the majority band. These characteristics can also be seen from the theoretical EDC's given in Fig. 2 for a number of $k_{\|}$ values. On a more quantitative level, the computed majority band intensity decreases by 60% as $k_{\|}$ decreases by 0.25 Å^{-1} below the Fermi momentum. The computed majority to minority intensity ratio at E_F of 1.7 compares well with the experimental ratio of 1.8.[36]

On the other hand, as expected, the Fermi surface (FS) radii and the dispersion of the majority- and minority-spin bands are not given correctly by the theory, representing the well-known limitations of the LSD approximation.[35,37] The computed majority and minority FS radii of $k_{\uparrow}=0.95$ Å^{-1} and $k_{\downarrow}=0.875$ Å^{-1} in Fig. 1 are smaller than the corresponding experimental values of 1.08 Å^{-1} and 0.96 Å^{-1}, respectively. Similarly, the theoretical dispersion is about twice as large as the measured one. The theoretical exchange splitting (in momentum) at E_F, $\Delta k=k_{\uparrow}-k_{\downarrow}=0.075$ Å^{-1}, is smaller than the experimental value $\Delta k=0.12$ Å^{-1}. These discrepancies can be ameliorated to varying degrees depending upon the choice of specifics of the computations. For example, the use of the experimental lattice constant (rather than the self-consistent LSD value obtained from the total-energy minimization used in this work), yields larger FS radii in much better accord with experiment. In this vein, the computed exchange splitting as well as dispersions could also be improved by invoking another exchange-correlation functional in determining the crystal potential. We have car-

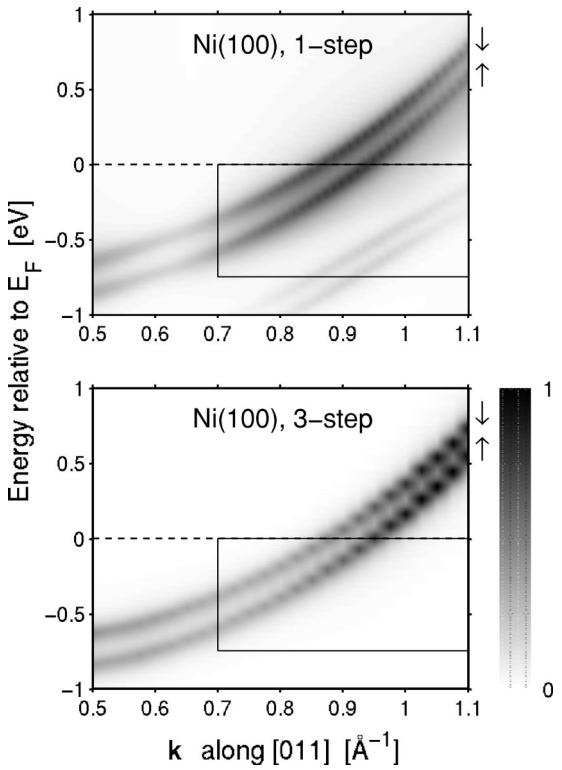

FIG. 3. Same as the caption to Fig. 1, except that this figure shows both the one-step (upper panel) and three-step (lower panel) theoretical ARPES intensities over a larger $k_\parallel$ range. Fermi function is not folded into the spectra. Rectangular box marks the region shown in Fig. 1(a).

ried out a number of such test computations and found that the key observations noted in the preceding paragraph concerning the theoretical spectra are robust to these uncertainties inherent in the first-principles band theory framework.

In connection with our use of $h\nu=43$ eV, even though the ARPES experiments in Fig. 1 are for $h\nu=44$ eV, we emphasize that we have made additional computations around this photon energy which indicate that for $h\nu$ values between 42 eV and 43.5 eV the computed spectra are essentially similar to those of Fig. 1(a). At photon energies lower than 42 eV, the distinctive high-intensity region in Fig. 1(a) or Fig. 3 moves below E_F for both spins. For $h\nu > 43.5$ eV, this intense feature moves above E_F, while a new high-intensity region emerges from below. With all this in mind, and the fact that our first-principles potentials probably do not locate the final states with an accuracy better than ~ 2 eV, the offset of ~ 1 eV used in our computations is considered quite reasonable.

Figure 3 considers one- and three-step ARPES intensities over a wider $k_\parallel$ range and gives insight into the nature of theoretical spectra. The Fermi cutoff has not been included so that the behavior of states above E_F can be explored. The one- and three-step results are seen in Fig. 3 to be essentially similar in that both display a region of high intensity with the intensity diminishing rapidly with decreasing $k_\parallel$ due to the presence of a band gap in the final-state spectrum. The details of the spectral intensity variations in the two cases are of course somewhat different because in the one-step case the final states and matrix elements do not enter[38] the calculation in the manner of Eq. (3). Notably, the one-step computation [Fig. 3(a)] shows a pair of surface states with a relatively low intensity lying below the bulk bands which are absent in the three-step model [Fig. 3(b)] where surface effects are not included.

Figure 3 emphasizes that the underlying character of the minority and majority band emissions is quite similar in that both contain the aforementioned region of high intensity. The main difference is that as a result of the exchange splitting, the region of intense emission moves to a higher energy for the minority band. Therefore, at the E_F, emission from the minority band is weaker compared to that of the majority band and the emitted electron beam is spin polarized. In this way, the rapid attenuation of intensity with increasing binding energy as well as the enhanced spin polarization of photoemitted electrons reported in Ref. 8 are both a consequence of the band gap in the final-state spectrum. Interestingly, even though the majority and minority bands lose intensity with decreasing $k_\parallel$ below E_F, both start to gain weight for $k_\parallel$ values below ≈ 0.6 Å^{-1}.

B. Salient features of the final-state bands, relevant transitions, and associated matrix elements

The right-hand side of the photointensity Eq. (3) makes it clear that the behavior of the computed ARPES spectra will be controlled by the specifics of the transitions involved and the associated matrix elements. These aspects of the initial and final states may be delineated with the help of Figs. 4 and 5. The filled circles with varying levels of darkness in Fig. 4 show the final-state bands as a function of $k_\perp$ for three typical values of $k_\parallel$ and differ considerably from the free-electron final-state bands shown by solid lines in Fig. 4(a) for reference. Note that these final-state bands apply to the majority as well as the minority states since the exchange splitting for the final states (~ 0.1 eV) is small compared to their broadening (~ 1 eV). The relevant initial-state majority and minority bands lifted by the photon energy (i.e., $E_i + h\nu$) are shown by dot-dashed lines. If the initial- and final-state widths related to Σ_i'' and Σ_f'' in Eq. (3) were infinitesimally small, then nonzero contributions to photointensity will only be possible from $k_\perp$ points where the initial- and final-state bands in Fig. 4 intersect. However, for typical values used in the computations (here, $\Sigma_i''=0.05$ eV, $\Sigma_f''=1.00$ eV), states within a few eV's of $E_i + h\nu$ overlap initial states through the tails of the final-state Lorentzians, and therefore, contributions to the photointensity can in principle arise from *all* $k_\perp$ points weighted by the transition matrix elements.

We see from Fig. 4 that for much of the $k_\parallel$ range of interest in Fig. 1 when the initial states are raised by the photon energy they lie in a band gap in the final-state spectrum, although at $k_\parallel=0.95$ Å^{-1} [Fig. 4(a)] $E_i + h\nu$ is very close to the final state f_b at $k_\perp \approx 0$. Notably the free-electron final state related to $\mathbf{G}=[200]$ (i.e., primary cone) crosses this region, as indicated by the crossed solid line in Fig. 4(a). There also are intersection points at $k_\perp$ around ± 0.7 Å^{-1} and at $\approx \pm 1.5$ Å^{-1}; these, however, are not important since the former involve secondary cone emissions which are

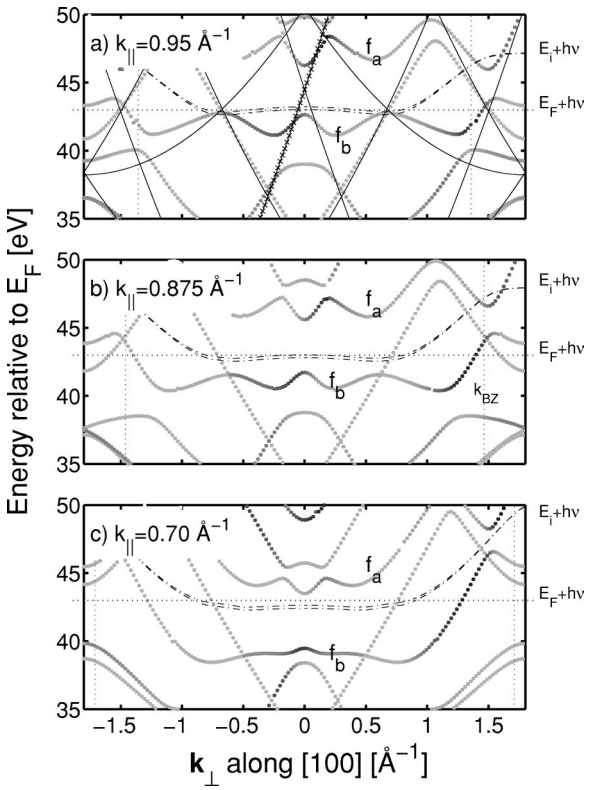

FIG. 4. Majority-spin final-state KKR band structure (dots) in Ni (small exchange splitting of ~0.1 eV in final states not shown) as a function of $\mathbf{k}_\perp$ along [100] for three different values of $\mathbf{k}_\parallel$ along [011]. The strength of the matrix element $M^{\sigma}_{f,\Sigma_1}(\mathbf{k}_\parallel,\mathbf{k}_\perp)$ between the majority Σ_1 initial-state band and the various final states is depicted by the degree of darkness of the dots. In (a), solid lines give the free-electron final states with the primary cone band highlighted with crosses. Dot-dashed lines give the dispersion of majority (lower lines) and minority (upper lines) initial-state bands lifted by the photon energy $h\nu=43$ eV (i.e., $E_i+h\nu$). The final-state bands f_a and f_b are the most relevant ones for the ARPES spectra analyzed in this work. Fermi level lifted by $h\nu$ is marked with a thin dotted horizontal line. The BZ boundaries which differ for various $k_\parallel$ values are marked by thin dotted vertical lines.

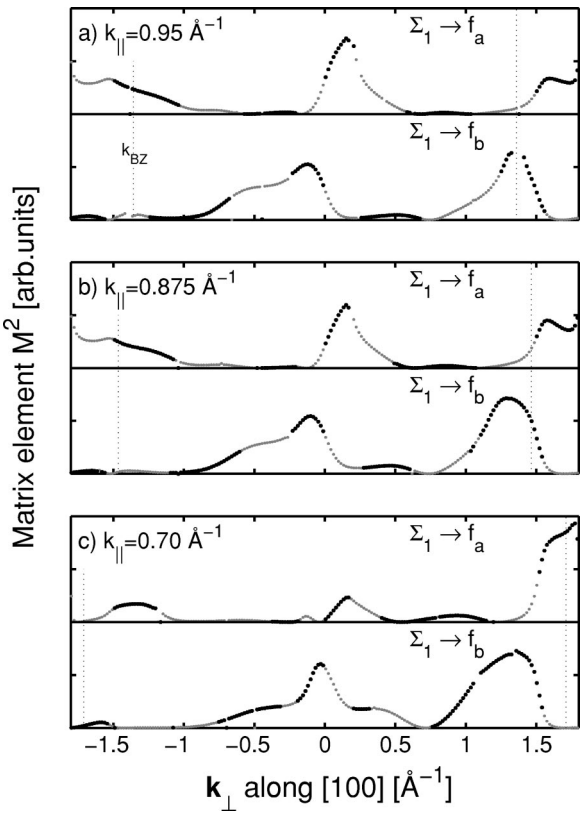

FIG. 5. Normalized photoemission matrix elements $M^{\sigma}_{f,\Sigma_1}(\mathbf{k}_\parallel,\mathbf{k}_\perp)^2$ for transitions from Σ_1 initial states to the final-state bands f_b and f_a as a function of $k_\perp$ for three different values of $k_\parallel$. The larger black dots indicate final states with a positive group velocity towards the surface. Thin vertical dotted lines indicate the BZ boundaries as in Fig. 4.

strongly attenuated as noted in Sec. II above, while the latter involve unoccupied states high above the E_F.[39] Keeping the remarks of the preceding paragraph in mind, the emissions arise therefore mainly from the Lorentzian tails of the two final-state bands f_a and f_b from the $k_\perp$ region around $k_\perp=0$.

But changes in the values of the matrix elements given by the degree of darkness of the final-state dots in Fig. 4 or in the more quantitative plots of Fig. 5 must also be considered. Recall from the discussion of Eq. (3) above that only photoelectrons traveling towards the surface are relevant; in Fig. 5, these $k_\perp$ regions are identified by the larger black dots. Different contributions to the photointensity are strongly modulated by the momentum dependence of the matrix element. At $k_\perp=0$, the matrix element for transition to the final state f_b is seen to decrease as a function of increasing $k_\parallel$, whereas the matrix element to f_a increases concomitantly. In fact, the sum of these two matrix elements remains practically the same, indicating that the spectral weight is transferred from f_b to f_a with increasing $k_\parallel$. The characteristic features of the ARPES spectra of Figs. 1–3 can be understood in terms of movements of the initial states in relation to the final-state bands f_a and f_b on the one hand, and changes in the matrix elements on the other.

C. Nature and origin of various spectral features

The discussion of the preceding section may be illustrated with the example of the EDC from Ni(100) at $k_\parallel=0.875$ Å^{-1}, where the minority-spin band crosses the E_F, shown in Fig. 6 together with its various components. The spin-resolved total intensities $I_\uparrow$ and $I_\downarrow$ arise mainly from transitions $\Sigma_1\rightarrow f_a$ and $\Sigma_1\rightarrow f_b$. Contributions from other transitions are quite small and are not shown. Note also that there is a small contribution at the position of the peak of either spin from the tail of the peak of the opposite spin. Referring to Figs. 4(b) and 5(b), note first that in Fig. 6 contributions from transitions to the final-state band f_a for the majority (dashed) as well as the minority (dotted) electrons arise mostly from the region $k_\perp\approx 0$. These two contributions are separated in energy due to the exchange splitting of the initial states; the minority curve possesses a slightly higher amplitude since the minority band lies closer to f_a.

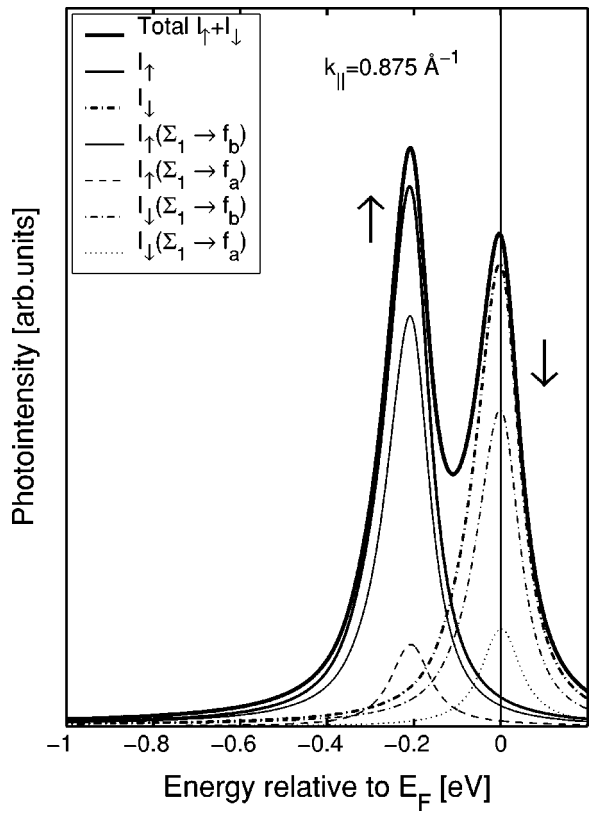

FIG. 6. Theoretical EDC of Fig. 2 for $k_\parallel = 0.875$ Å^{-1} is shown decomposed into majority- and minority-spin contributions. For each spin, contributions from $\Sigma_1 \rightarrow f_a$ and $\Sigma_1 \rightarrow f_b$ are given. See legend for meaning of various line styles.

The situation with f_b is similar. The lifted initial states, however, lie closer to f_b than f_a, so that the overall amplitude of the transitions to f_b is higher than to f_a. Moreover, the majority contribution (thin solid) is higher than the minority one (thin chain) since the majority band lies closer to f_b.

The EDC's at other $k_\parallel$ values can be analyzed along the lines of the preceding paragraph. Although a detailed discussion will be repetitious, some comments on the $k_\parallel$ dependencies of Figs. 2 and 3 are appropriate. As $k_\parallel$ decreases in Fig. 2 below 0.95 Å^{-1}, the majority as well as the minority peak intensities decrease because the initial states move further away from f_b as seen in Fig. 4. This is due to the larger dispersion (as a function of $k_\parallel$) of the final states f_a and f_b compared to the initial states. Although the initial states at the same time move closer to f_a, the net contribution from f_a does not change much since the matrix element for f_a decreases simultaneously. For $k_\parallel$ values greater than 0.95 Å^{-1} in Fig. 3, the initial (unoccupied) states begin to intersect f_b and the intensity increases. It is clear then that the rapid decrease in intensity near E_F in the majority or the minority band in Fig. 3 results from the presence of a band gap between f_a and f_b around $k_\perp = 0$. Incidentally, for $k_\parallel$ values less than 0.6 Å^{-1}, one begins to intersect f_a and other final states. For $k_\parallel$ values greater than 0.80 Å^{-1} in Fig. 2, the majority feature is more intense than the minority one since the majority band energetically lies closer to f_b.

We turn now to address the issue of the final-state width (full width at half maximum), which is given by $2\Sigma_f''$. For electron energies around 40 eV, the early results of Ref. 40 which are based on an analysis of the low-energy electron-diffraction data from Ni suggest $\Sigma_f'' \approx 3$ eV. Other studies[34,41–43] in Cu, including a recent one-step computation of ARPES spectra for emission from the E_F in Cu(100),[44] indicate smaller Σ_f'' values ranging from 1.8 eV to 3 eV. In this connection, we have carried out extensive simulations using different values of Σ_f''. We find that it is difficult to obtain the abrupt reduction in the majority-spin band intensity seen in the experimental ARPES spectra of Fig. 1(b) for Σ_f'' values much larger than ~1.5 eV. For $\Sigma_f'' \sim 3$ eV, the onset of the band gap in Fig. 1(a) or 3 becomes rather diffuse and the differences between the majority and minority band intensities become small. The key parameter here is the value of Σ_f'' in relation to the size of the final-state gap Δ: For $\Sigma_f'' < \Delta/2$, the final-state gap induces a significant modulation in the photointensities, but for $\Sigma_f'' \geqslant \Delta$, little variation in intensity occurs when the gap is traversed. The fact that we obtain such a good level of agreement with experiments using $\Sigma_f'' = 1$ eV in *both* one-step and three-step computations seems to suggest that the final states involved under the measurement conditions of Ref. 8 considered in this work possess enhanced lifetimes. This is however not clear because, as already noted, the LSD possesses limitations in describing the initial-state dispersion and exchange splitting in the ground state. These shortcomings will, if anything, be accentuated when it comes to the final-state band gaps and dispersions. Therefore, our effective value of $\Sigma_f'' = 1$ eV may alternatively indicate that the final-state gap is underestimated by a few eV's in our computations. Incidentally, the increase in the lifetime of the photohole with increasing binding energy is not a significant factor here.[45] Further experimental work to pin down the nature of the final states in Ni would be worthwhile in clarifying this point.

D. $\mathbf{k}_\parallel$ and $\mathbf{k}_\perp$ dependence of initial-state character

The role of the initial-state character in the present ARPES spectra bears some comment. For this purpose, Fig. 7 gives the $k_\parallel$ dependence of the spin-polarized band structure of Ni for $k_\perp = 0$, while Fig. 8 gives the $k_\perp$ dependence for $k_\parallel = 0.875$ Å^{-1}, together with the *s*, *p*, and *d* weights in the wave function of the Σ_1 band. The bands of Fig. 8, which are along a line offset from the BZ center, should be distinguished from the more familiar band-structure plots along high-symmetry lines in the BZ. We see first that there is little difference between the characters of the majority and minority states at any **k** point. As one moves away from the zone center, the *d* character of the Σ_1 band decreases at the expense of an increasing *s*-*p* character. At $k_\parallel = 0.95$ Å^{-1} in Fig. 7 where the majority band crosses the E_F, Σ_1 states are still largely *d* like. Between $k_\parallel = 0$ and 0.95 Å^{-1}, the *d* component decreases by 6% and over the region of rapid variation in the majority ARPES intensity in Fig. 1(a) where $k_\parallel$ increases from 0.80 Å^{-1} to 0.95 Å^{-1}, the *d* component decreases by only 3%. Moreover, for these $k_\parallel$ values, the *d*

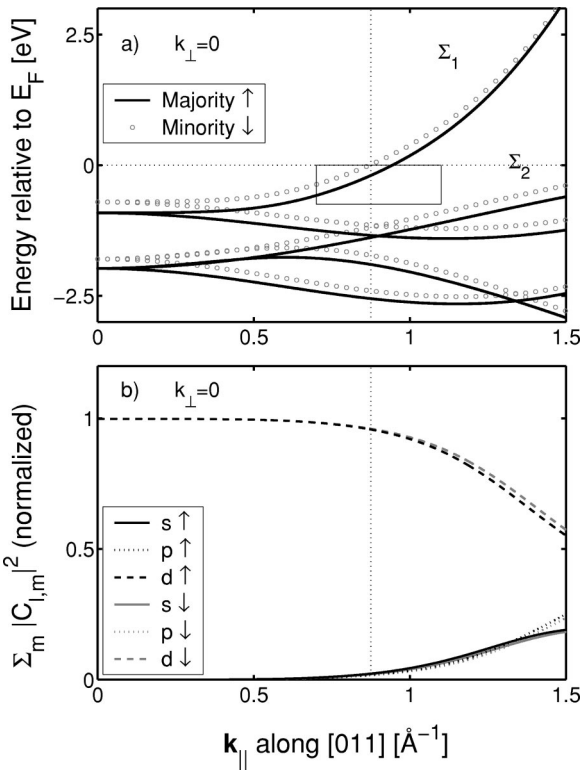

FIG. 7. (a) Majority and minority initial-state bands as a function of $\mathbf{k}_\parallel$ along the [011] direction (i.e., along Γ-K-X) at $k_\perp = 0$. The energy is relative to the Fermi energy. Region of the Σ_1 band shown in Fig. 1(a) is highlighted with the rectangular box. (b) Normalized weights $\Sigma_m |C_{l,m}|^2$ for different l values where $C_{l,m}$ are the wave function coefficients of the Σ_1 band for angular and magnetic quantum numbers l and m. See legend for meaning of various line types. Vertical dotted line marks the $k_\parallel$ position (0.875 Å^{-1}) where the minority Σ_1 band crosses E_F.

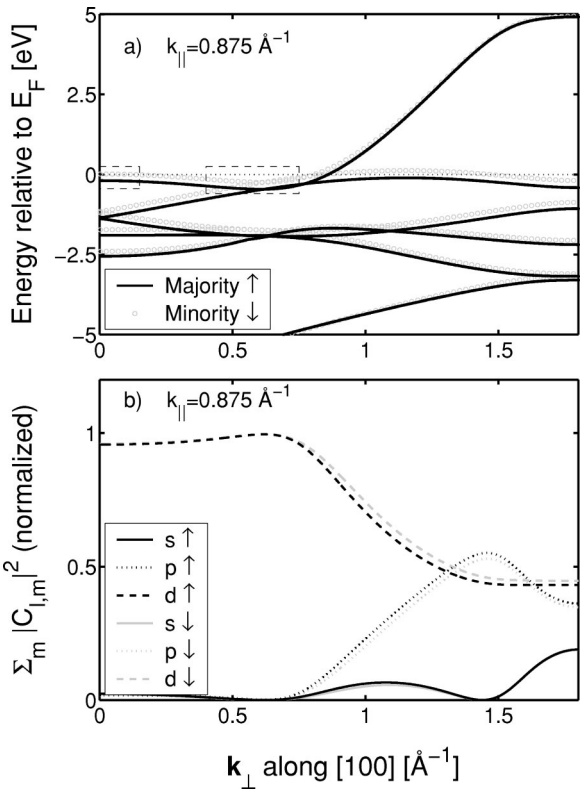

FIG. 8. Same as the caption to Fig. 7, except that these figures show variations as a function of $\mathbf{k}_\perp$ along [100] with $k_\parallel$ held fixed at 0.875 Å^{-1} where the minority Σ_1 band crosses the E_F (i.e., the dotted vertical line in Fig. 7). In (a), the box around $k_\perp = 0$ denotes the region of primary cone emission, while the other box roughly indicates the region of secondary cone emissions discussed in the text.

character remains large as a function of $k_\perp$ for both the primary and secondary cone emission regions shown by rectangular boxes in Fig. 8 around $k_\perp \approx 0$ Å^{-1} and 0.65 Å^{-1}; if anything, the d character increases slightly up to $k_\perp \approx 0.75$ Å^{-1}. On the other hand, the dispersion and character of the final-state bands f_a and f_b (see Fig. 4) vary substantially as a function of $k_\parallel$ and/or $k_\perp$. These considerations indicate that changes in the initial-state character play a relatively small role in accounting for those in the matrix elements of Fig. 5 or in the ARPES intensities of Fig. 1.

V. SUMMARY AND CONCLUSIONS

We have carried out extensive one-step- and three-step-type ARPES computations on Ni(100) within the spin-resolved band theory framework using the LSD approximation to treat exchange-correlation effects. Much of our analysis is based on the three-step calculations for the ease of interpretation, although the one-step computations yield similar conclusions. The results provide considerable insight into the recent high-resolution ARPES experiments of Ref. 8 on Ni(100) which probe the majority- and minority-spin Σ_1 band along the Γ-K direction near the E_F with 44 eV photons. A good overall level of accord between theory and experiment is seen: The one-step as well as the three-step computations reproduce the dramatic observed variations with $\mathbf{k}_\parallel$ in the *majority* band photointensity on the one hand and a relatively smoother variation of the *minority* intensity on the other. The $\mathbf{k}_\parallel$ and energy dependencies of various spectral features are analyzed in terms of the behavior of the initial and final states and changes in the relevant transition matrix elements. The final states display substantial dispersion as a function of $\mathbf{k}_\parallel$ at a fixed $\mathbf{k}_\perp$ or as a function of $\mathbf{k}_\perp$ for a given $\mathbf{k}_\parallel$ and possess an energy gap. The associated matrix elements undergo large variations with $\mathbf{k}_\parallel$ and $\mathbf{k}_\perp$, but the changes in the character of the initial states over the energy and momentum region of interest are relatively small. Remarkable decrease observed in the ARPES intensity of the majority-spin Σ_1 band as it disperses below the E_F as well as the enhanced spin polarization of the photoemitted electrons at the E_F arises primarily from the presence of a band gap in the final-state spectrum under the experimental conditions of Ref. 8.

Despite the uncertainties inherent in the first-principles LSD framework with respect to the dispersion and placement of the initial- and final-state bands and the exchange splitting, and the fact that correlation effects beyond the LSD are undoubtedly at play in Ni, this study shows that by making reasonable choices of various computational parameters, one

is able to adduce a good understanding of the ARPES spectra investigated. Notably, our preliminary computations on Ni(110) and Cu(100) reproduce the characteristic differences in the intensity variations between Ni(100), Ni(110), and Cu(100) reported by Ref. 8. Further high-resolution ARPES work along these lines over a wider range of photon energies and $\mathbf{k}_\parallel$ values would prove valuable in characterizing single- as well as many-particle aspects of the initial and final states.

ACKNOWLEDGMENTS

It is a pleasure to acknowledge important conversations with Franz Himpsel who suggested that we look into the spin-polarized ARPES intensities from Ni(100) in view of recent experimental advances. We thank Kyle Altmann for comments on the manuscript. This work was supported by the US Department of Energy Contract No. W-31-109-ENG-38, and benefited from the allocation of supercomputer time at the NERSC, the Northeastern University Advanced Scientific Computation Center (ASCC), and the Institute of Advanced Computing (IAC). One of us (S.S.) acknowledges Suomen Akatemia, Vilho, Yrjö ja Kalle Väisälän Rahasto, Tekniikan Edistämissäätiö, and Jenny ja Antti Wihurin Rahasto for financial support.

APPENDIX A: KKR FORMULATION OF MOMENTUM MATRIX ELEMENT FOR A GENERAL LATTICE

It is useful to first cast the standard KKR description for complex lattices[46,47,27] into a form wherein the positive and negative energies are treated on an equal footing. The trial wave function ψ for a system of nonoverlapping muffin tins can be expanded in terms of the real spherical harmonics $Y_L(\Omega)$ as:[48]

$$\psi(\mathbf{r}) = \sum_{\beta,L} i^l C_L^{(\beta)} R_l^{(\beta)}(r) Y_L(\Omega) \tag{A1}$$

$$\equiv \sum_{\beta} \psi^{(\beta)}, \tag{A2}$$

where L denotes the angular quantum indices (l,m), $R_l^{(\beta)}(r)$ is the regular solution of the radial Schrödinger equation for the basis atom β and $C_L^{(\beta)}$ is the associated variational coefficient. It is convenient to introduce quantities $\psi^{(\beta)}$ defined by Eq. (A2) when the momentum matrix element is evaluated below. The radial solutions $R_l^{(\beta)}(r)$ are chosen to reduce to spherical Bessel functions in the limiting case of an empty lattice.

We now express the KKR Green function in the empty lattice limit (i.e., for free particles with boundary conditions appropriate for a periodic lattice) using the spherical Bessel and Neumann functions (here and frequently elsewhere the site indices β are suppressed in the interest of simplicity) as follows:[49,50]

$$G(\mathbf{r},\mathbf{r}') = \sum_{L,L'} \{A'_{L,L'} j_l(\kappa r) j_{l'}(\kappa r')^* + \kappa \delta_{L,L'} j_l(\kappa r') n_l(\kappa r')\} Y_L(\Omega) Y_{L'}(\Omega'), \tag{A3}$$

where the solution of the homogeneous equation (i.e., the first term) is taken explicitly to be of the form $D \equiv \psi\psi^*$. For positive energies, form (A3) is identical to the standard KKR formulation; however, for negative energies, this form differs in a subtle but important manner via the presence of the complex conjugate ψ^* in D. The use of Eqs. (A1) and (A3) yields then the KKR variational functional,

$$\Lambda_{MT} = -\sum_{L,L'} C_L^* [R_l'^* j_l - R_l^* j_l'] r^2 \times \left\{ i^{l'-l} A'_{L,L'} + \kappa \delta_{L,L'} \frac{n_l' - \frac{R_l'}{R_l} n_l}{j_l'^* - \frac{R_l'}{R_l} j_l^*} \right\} \times r^2 [R'_{l'} j_{l'}^* - R_{l'} j_{l'}'^*] C_{L'}. \tag{A4}$$

Setting

$$\hat{C}_L \equiv r^2 [R_l' j_l^* - R_l j_l'^*] C_L, \tag{A5}$$

the elements of the secular matrix $\Lambda_{L,L'}$ are identified as the expression in the curly brackets on right side of Eq. (A4). Since Λ_{MT} satisfies the form of the KKR functional, the usual steps to obtain the energy bands and wave functions can be followed. This formulation can be used seamlessly over the whole energy range without requiring a separate consideration of positive and negative energies as is the common practice. Finally, it can be shown that the matrix $A'_{L,L'} \propto (j_l j_{l'}^*)^{-1}$ is related to the standard KKR structure constants $A_{L,L'}$ via

$$A'_{L,L'} = A_{L,L'}, \quad E>0 \qquad = (-1)^{l'} A_{L,L'}, \quad E<0. \tag{A6}$$

We consider next the momentum matrix element defined as the matrix element of the momentum operator between one-particle electronic states Ψ_n and $\Psi_{n'}$ within LSD,

$$\mathbf{p}_{n',n} = \langle \Psi_{n'}(\mathbf{k}) | \mathbf{p} | \Psi_n(\mathbf{k}) \rangle = \frac{1}{N} \int_V \Psi_{n'}^* \mathbf{p} \Psi_n d\mathbf{r}, \tag{A7}$$

where the multiplier $1/N$ is due to the normalization of the wave function to unity within the Wigner-Seitz unit cell. Decomposing the integral into a part over the various muffin-tin sphere volumes $V^{(\beta)}$ within the central Wigner-Seitz cell (via use of Bloch's theorem) and into another part over the remaining interstitial space V' yields

$$\mathbf{p}_{n',n} = \sum_{\beta} \int_{V^{(\beta)}} \psi_{n'}^{(\beta)*} \mathbf{p} \psi_n^{(\beta)} d\mathbf{r} + \frac{1}{N} \int_{V'} \Phi_{n'}^* \mathbf{p} \Phi_n d\mathbf{r}, \tag{A8}$$

where $\psi^{(\beta)}$ and Φ denote parts of the wave function inside and outside the muffin tins, respectively. Green's theorem can be used to cast the second term into the form

$$\int_{V'} \Phi_{n'}^{*} \mathbf{p} \Phi_n d\mathbf{r} = N \frac{\hbar^2}{2m(E_{n'} - E_n)} \sum_{\alpha} \hat{\mathbf{e}}_{\alpha} \int_{S'} (\Phi_{n'}^{*} \nabla p_{\alpha} \Phi_n - p_{\alpha} \Phi_n \nabla \Phi_{n'}^{*}) \cdot d\mathbf{S}, \tag{A9}$$

where the surface integral is over the nonoverlapping muffin-tin surfaces of the atoms in the basis and much of the notation is obvious. $\hat{\mathbf{e}}_{\alpha}$ are the Cartesian unit vectors, i.e., $\alpha \equiv x,y$ or z and p_{α} are the corresponding components of the momentum operator. The surface integral can now be carried out by replacing the wave function Φ_i by ψ,

$$\mathbf{p}_{n',n} = \sum_{\beta} \sum_{\alpha} \hat{\mathbf{e}}_{\alpha} \left\{ \int_{V^{(\beta)}} \psi_{n'}^{(\beta)*} p_{\alpha} \psi_n^{(\beta)} d\mathbf{r} + \frac{\hbar^2}{2m(E_{n'} - E_n)} \int_{S^{(\beta)}} (\psi_{n'}^{(\beta)*} \nabla p_{\alpha} \psi_n^{(\beta)} - p_{\alpha} \psi_n^{(\beta)} \nabla \psi_{n'}^{(\beta)*}) \cdot d\mathbf{S} \right\} \tag{A10}$$

$$= \sum_{\beta} \mathbf{p}_{n',n}^{(\beta)}. \tag{A11}$$

The second equation defines the contribution of various basis atoms to the momentum matrix element in a complex lattice.

The evaluation of the quantities $\mathbf{p}_{n',n}^{(\beta)}$ can be carried out much along the lines used for simple lattices[51,52] by inserting form (A1) for the wave functions into Eqs. (A10) and (A11) as

$$\mathbf{p}_{n',n}^{(\beta)} = \sum_{\alpha} \hat{\mathbf{e}}_{\alpha} \sum_{L,L'} i^{l-l'-1} C_{L'}^{(\beta)*} C_L^{(\beta)} B_{l,l'}^{(\beta)} \mathcal{G}_{L,L'}^{\alpha}, \tag{A12}$$

where the primed indices refer to the final states. $B_{l,l'}^{(\beta)}$ is the radial contribution. $\mathcal{G}_{L,L'}^{\alpha}$ are of the form of Gaunt coefficients involving integrals of products of three real spherical harmonics. Due to selection rules, $B_{l,l'}^{(\beta)}$ are needed only for $l' = l \pm 1$ and are given by equations slightly modified from those of Ref. 52. Our radial wave functions $R_l^{(\beta)}(r)$ relate to the radial functions $P_l(r)$ of Ref. 52 via: $R_l^{(\beta)}(r) \equiv r^{-1} P_l^{(\beta)}(r)$. Also, all wave functions related to primed states in Eqs. (7)–(8) of Ref. 52 must be complex conjugated. Detailed expressions are obtained straightforwardly.

[1] See, e.g., F.J. Himpsel, J.E. Ortega, G.J. Mankey, and R.F. Willis, Adv. Phys. **47**, 511 (1998).

[2] P. Aebi, T.J. Kreutz, J. Osterwalder, R. Fasel, P. Schwaller, and L. Schlapbach, Phys. Rev. Lett. **76**, 1150 (1996).

[3] W. Kuch, A. Dittschar, K. Meinel, M. Zharnikov, C.M. Schneider, J. Kirschner, J. Henk, and R. Feder, Phys. Rev. B **53**, 11 621 (1996).

[4] D.M.C. Nicholson, W.H. Butler, W.A. Shelton, Y. Wang, X.-G. Zhang, and J.M. MacLaren, J. Appl. Phys. **81**, 4023 (1997).

[5] T.J. Kreutz, T. Greber, P. Aebi, and J. Osterwalder, Phys. Rev. B **58**, 1300 (1998).

[6] D.Y. Petrovykh, K.N Altmann, H. Höchst, M. Laubscher, S. Maat, G.J. Mankey, and F.J. Himpsel, Appl. Phys. Lett. **73**, 3459 (1998).

[7] M. Hochstrasser, N. Gilman, R.F. Willis, F.O. Schumann, J.G. Tobin, and E. Rotenberg, Phys. Rev. B **60**, 17 030 (1999).

[8] K.N. Altmann, D.Y. Petrovykh, G.J. Mankey, N. Shannon, N. Gilman, M. Hochstrasser, R.F. Willis, and F.J. Himpsel, Phys. Rev. B **61**, 15 661 (2000).

[9] C. Pampuch, O. Rader, R. Kläsges, and C. Carbone, Phys. Rev. B **63**, 153409 (2001).

[10] P.E. Mijnarends, S. Sahrakorpi, M. Lindroos, and A. Bansil, Phys. Rev. B **65**, 075106 (2002).

[11] J.B. Pendry, Surf. Sci. **57**, 679 (1976).

[12] J.F.L. Hopkinson, J.B. Pendry, and D.J. Titterington, Comput. Phys. Commun. **19**, 69 (1980).

[13] M. Lindroos and A. Bansil, Phys. Rev. Lett. **75**, 1182 (1995).

[14] M. Lindroos and A. Bansil, Phys. Rev. Lett. **77**, 2985 (1996).

[15] A. Bansil and M. Lindroos, Phys. Rev. Lett. **83**, 5154 (1999).

[16] W.E. Spicer, Phys. Rev. **112**, 114 (1958).

[17] C.N. Berglund and W.E. Spicer, Phys. Rev. **136**, A1030 (1964).

[18] P.J. Feibelman and D.E. Eastman, Phys. Rev. B **10**, 4932 (1974).

[19] J.F. Janak, A.R. Williams, and V.L. Moruzzi, Phys. Rev. B **11**, 1522 (1975).

[20] W.D. Grobman, D.E. Eastman, and J.L. Freeouf, Phys. Rev. B **12**, 4405 (1975).

[21] M. Cardona and L. Ley, *Photoemission in Solids I: General Principles* (Spinger-Verlag, Berlin, 1978).

[22] C. Kunz in *Photoemission in Solids II*, edited by L. Ley and M. Cardona (Springer-Verlag, Berlin, 1979), p. 313.

[23] J.E. Inglesfield and E.W. Plummer, in *Angle Resolved Photoemission, Theory and Current Applications*, edited by S.D. Kevan (Elsevier, Amsterdam, 1992).

[24] M. Lindroos, Phys. Scr. **25**, 788 (1982).

[25] G.D. Mahan, Phys. Rev. B **2**, 4334 (1970).

[26] P.E. Mijnarends and L.P.L. Rabou, J. Phys. F: Met. Phys. **16**, 483 (1986).

[27] P.E. Mijnarends and A. Bansil, J. Phys.: Condens. Matter **2**, 911 (1990).

[28] U. von Barth and L. Hedin, J. Phys. C **5**, 1629 (1972).

[29] A.K. Rajagopal and J. Callaway, Phys. Rev. B **7**, 1912 (1973).

[30] A. Bansil and S. Kaprzyk, Phys. Rev. B **43**, 10 335 (1991).

[31] S. Kaprzyk and A. Bansil, Phys. Rev. B **42**, 7358 (1990).

[32] A. Bansil, S. Kaprzyk, P.E. Mijnarends, and J. Tobola, Phys. Rev. B **60**, 13 396 (1999).

[33] J. Hermanson, Solid State Commun. **22**, 9 (1977).

[34] J.A. Knapp, F.J. Himpsel, and D.E. Eastman, Phys. Rev. B **19**, 4952 (1979).

[35] See, e.g., W. Nolting, W. Borgiel, V. Dose, and Th. Fauster, Phys. Rev. B **40**, 5015 (1989).

[36] Such a quantitative level of agreement between theoretical and experimental results should perhaps be considered fortuitous in view of limitations inherent to Eq. (3) for modeling photointensities.

[37] See, e.g., R.G. Parr and W. Yang, *Density-Functional Theory of Atoms and Molecules* (Oxford University Press, Oxford, London, 1989).

[38] The final states in our one-and three-step computations are identical if the photoelectron is assumed to have zero damping. However, for finite damping, the final states in the one-step calculation undergo energy shifts not present in the three-step formulation of Eq. (3). This results in some differences between the one-and three-step photointensities in Fig. 3.

[39] The secondary cone emissions are greatly attenuated in the one-step computations. We have incorporated this constraint in the present three-step calculation by restricting the $k_\perp$ range in Eq. (3) to $[-0.4,+0.4]$ Å^{-1} so that the secondary cone emission is essentially excluded; the precise $k_\perp$ range used is not important so long as the region near $k_\perp \approx 0.7$ Å^{-1} is excluded.

[40] J.E. Demuth, P.M. Marcus, and D.W. Jepsen, Phys. Rev. B **11**, 1460 (1975).

[41] A. Goldmann, W. Altmann, and V. Dose, Solid State Commun. **79**, 511 (1991).

[42] V.N. Strocov, H.I. Starnberg, and P.O. Nilsson, J. Phys.: Condens. Matter **8**, 7539 (1996).

[43] R. Courths, S. Löbus, S. Halilov, T. Scheunemann, H. Gollisch, and R. Feder, Phys. Rev. B **60**, 8055 (1999).

[44] M. Lindroos, J. Avila, M.E. Davila, Y. Huttel, M.C. Asensio, and A. Bansil, Surf. Sci. **482-485**, 718 (2001).

[45] In particular, Ref. 8 notes that the decrease in spectral intensity is accompanied with relatively small increase in widths of spectral peaks. We have carried out simulations in which the initial-state lifetime was taken to be energy dependent following the results of Ref. 34. Consistent with the analysis of Ref. 8, our conclusion also is that the photohole lifetime is not a significant factor for the observed drastic drop in the photointensity, although the use of an energy-dependent lifetime (after Ref. 34) would yield a somewhat improved agreement between theory and experiment.

[46] W. Kohn and N. Rostoker, Phys. Rev. **54**, 1111 (1954).

[47] F.S. Ham and B. Segall, Phys. Rev. **124**, 1786 (1961).

[48] See, e.g., H.L. Davis, in *Computational Methods in Band Theory*, edited by P.M. Marcus, J.F. Janak, and A.R. Williams (Plenum Press, New York, 1971).

[49] P.T. Landsberg, *Solid State Theory-Methods and Applications* (Wiley-Interscience, New York, 1969).

[50] J. Callaway, *Quantum Theory of the Solid State* (Academic Press, New York, 1976).

[51] A.B. Chen, Phys. Rev. B **14**, 2384 (1976).

[52] N.A. Shilkova and V.P. Shirikovskii, Phys. Status Solidi B **146**, 173 (1988).